University of Pennsylvania
Team 7 - Jason Chen, Solomon Gonzalez, Leo Tan

MEAM 5270 Final Report
May 4, 2025

Structural Failure Analysis of High-Mounted F1 Airfoils: A COMSOL-Based Case Study of the 1969 Lotus 49B

Table of Contents

1 Introduction

The use of aerodynamic devices and geometry in motorsports evolved gradually throughout the early to mid-20th century. While aircraft designers have long understood the principles of lift and drag through airfoil theory, racing applications initially focused on streamlining the race car rather than generating downforce [1]. The first notable implementation of an aerodynamic wing in motorcycle racing came from Jim Hall's Chaparral 2E, as shown in Figure 1, which debuted in 1966. This groundbreaking design generated downforce to improve grip when cornering, fundamentally changing racing aerodynamics.

Figure 1: Jim Hall's Chaparral 2E, the first elevated wing mounted on struts [2]

Formula 1 (F1) teams quickly adapted this technology and experimented with various wing configurations. The Lotus 49, designed by Colin Chapman, marked the change from modest installations to increasingly extreme configurations as their wings were mounted several feet above the cars on tall, slender struts [3]. The original intention with these designs was to capture clean, undisturbed airflow, maximizing their effectiveness. However, the structural vulnerabilities of such a design was overlooked.

Figure 2: Lotus 49B

During the Spanish Grand Prix at Montjuic Park on May 4th, 1969, Graham Hill's Lotus 49B suffered a catastrophic rear wing structural failure when the supporting strut broke while cresting a rise on the track. The supports of the rear wing collapsed under extreme aerodynamic load, causing Hill to lose control and crash heavily into the barriers. Although incident reports did not specify the exact failure mechanism, engineering analysis supports two primary possibilities: either compressive buckling of the slender aluminum struts under substantial downforce, or failure due to the moment created by drag forces acting on the wing's center of pressure. Though Hill survived the incident, it highlighted the dangerous experimental nature of the early high-mounted wings in F1. These failures were not isolated incidents as similar structures had collapsed on other teams' cars, sparking emergency action and regulation from the governing body by banning high-mounted wings effective immediately before the Monaco Grand Prix two weeks later. This marked one of the first major safety-driven regulatory interventions in F1 aerodynamics, establishing a precedent for modern F1 racing.

This study aims to recreate and analyze the aerodynamic forces and resulting torques that contributed to these failures by using computational fluid dynamics (CFD) in COMSOL Multiphysics. By examining the interactions between fluid dynamics and structural limitations, conditions that led to these historical failures are investigated and conclusions on engineering insights applicable to modern high-downforce aerodynamic design are drawn.

2 Methodology

Our analysis employs a systematic approach to investigate the aerodynamic forces and structural limitations of the high-mounted wings used on the 1969 Lotus 49B. To manage computational complexity while maintaining physical relevance, the following simplifications were made:

2.1 Dimensional Reduction

Rather than simulating the full three-dimensional wing, a two-dimensional airfoil cross section analysis is conducted. This approach significantly reduces the computational demands while still capturing the essential flow physics responding for generating lift, drag, and the resulting moments on the supporting structure.

2.2 Airfoil selection

For the analysis, the NACA 0012 airfoil profile has been selected. While the exact cambered profile used in the Lotus 49B is not well documented due to secrecy in competitive racing, it was estimated that the most likely airfoil to have been used was the NACA 0012 [4]. This serves as a well-documented baseline with extensive validation data from the NACA airfoil database, allowing for validation of the simulation methodology against established experimental results [5].

2.3 Support structure

Instead of modeling the complex multi-strut arrangement used on the Lotus 49B, the analysis has been simplified to focus on a single support point. This allows for the calculation of the total torque applied to the structure while avoiding complexities of load distribution across multiple attachment points and an underdetermined system of equations.

2.4 Domain configuration

A C-shape computational domain with the airfoil positioned near the bottom left region is employed. This configuration efficiently models the external air flow while making the curvature of the grid match the leading edge of the airfoil, ensuring better flow separation [6]. Additionally, 10, 10, and 20 chord lengths are selected for the upstream, vertical, and downstream clearance respectively. This allows for undisturbed flow development, preventing artificial acceleration effects, and captures the wake effect.

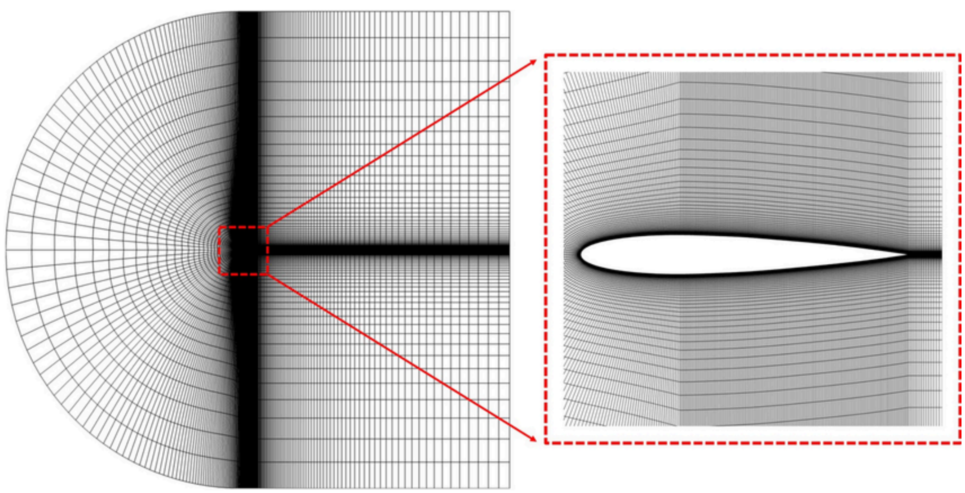

Figure 3: Typical C-shape domain

2.5 Analysis framework

The investigation follows a dual analytical approach as follows:

1. Validating the computational results against published NACA airfoil data to verify stall characteristics, overall lift and drag performance trends, and quantify simulation accuracy through rigorous error metrics.
2. Upon validating the computational results, the highest calculated aerodynamic forces are then applied to perform a failure mode analysis of the wing support system. Given that the failure occurred due to either buckling or bending, downforce and drag force will be derived for each configuration. A free body diagram (FBD) is created to represent the airfoil with a singular support structure in which dynamics will be implemented:

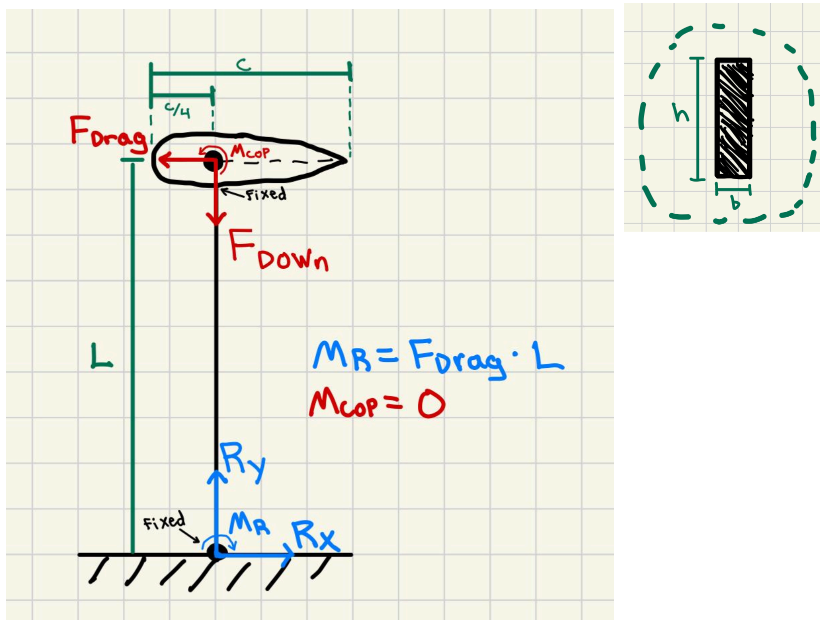

Figure 4: FBD of System and Support Cross-section

2.6 Failure Mode Analysis

As the dimensions of the supports are not reported, these approximations will be made from known dimensions and the image in Figure 1: L = 1.2m, b = 0.01m, h = 0.07m. It is assumed that the supports were made from 2024 aluminum, an alloy commonly used in F1 vehicle framing around the 1960s with a Young's Modulus of 70GPa and a yield strength of 324 MPa [5][6].

2.6.1 Buckling Analysis

The critical load determines when a given column will buckle under a compressive force, and is calculated using this equation:

Critical load eq

The moment of inertia of

Using the COMSOL derived values, force and moment balances are performed to determine if the support structure will fail under these loading conditions upon comparison with known material properties of the aluminium status used in the 1969 Lotus 49B.

3 COMSOL Implementation

This section will highlight the implementation of the simulation framework in COMSOL Multiphysics, documenting the model parameters, physics interface, and boundary conditions used to analyze the aerodynamic behavior of the high-mounted F1 airfoil.

3.1 Global variable definition

The simulation framework is built upon defined global variables that ensure consistency across all analyzes as shown in Figure 5.

Name	Expression	Value	Description
Re	rho_inf*U_inf*c/mu_inf	6.125E6	Reynolds number
c	1[m]	1 m	Chord length of airfoil
r_halfcircle	10[m]	10 m	Radius of C shape domain's left semi circle
r_circle	1[m]	1 m	Radius of rotation circular domain over the airfoil
alpha	0	0	Angle of attack
om_inf	10*U_inf/L_rectangle	45 1/s	Free-stream specific dissipation rate
k_inf	0.1*mu_inf*U_inf/(rho_inf*L_rectangle)	6.6122E-6 m^2/s^2	Free-stream turbulent kinetic energy
L_rectangle	20[m]	20 m	Side length of C shape domain's rectangle
mu_inf	1.8e-5[kg*m^-1*s^-1]	1.8E-5 kg/(m·s)	Dynamic viscosity of air
rho_inf	1.225[kg*m^-3]	1.225 kg/m^3	Density of air
U_inf	90[m*s^-1]	90 m/s	Inflow velocity

Figure 5: COMSOL global variables

3.2 Components

The simulation geometry consists of a nested domain structure designed to facilitate angle of attack variations without altering the inflow boundary conditions. This features an inner circular domain with radius c centered around the NACA 0012 airfoil, encapsulated within a larger C-shaped fluid domain extending 10 chord lengths upstream, above, and below the airfoil, and 20 chord lengths downstream. The NACA 0012 profile was imported as a parametric curve with the center of pressure (quarter chord) positioned at the center of the circular subdomain. This configuration offers significant advantages for our parametric study as it allows for the airfoil to be rotated within the circular domain without affecting the external boundaries. Not only does this offer a straightforward way in conducting the parametric study, it also allows for a consistent reference frame for post-processing and force calculations as the angle of attack changes.

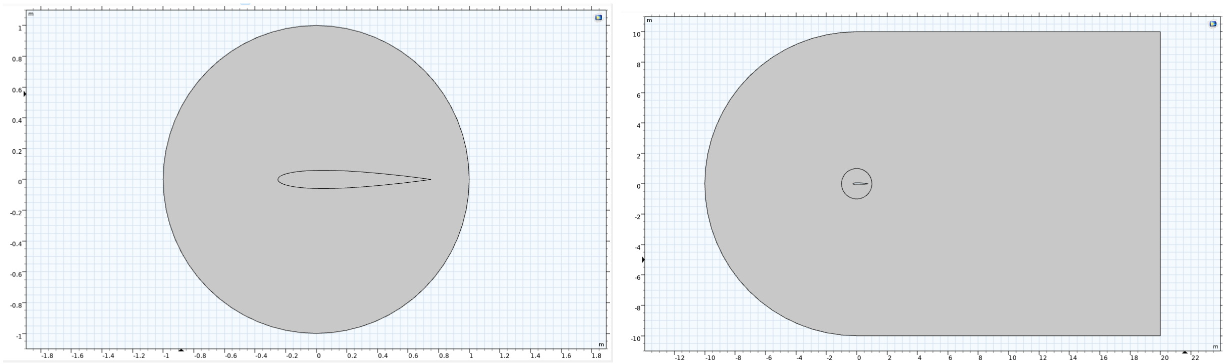

Figure 6: Circular domain centered around the NACA 0012 airfoil's center of pressure (left) and complete domain (right)

Air is defined as the domain material with standard properties as follows:

1. Density: $\rho = 1.225 \frac{kg}{m^3}$
2. Dynamic viscosity: $\mu = 1.8 \cdot 10^{-5} \frac{kg}{m \cdot s}$

3.3 Model

Within COMSOL Multiphysics, the $k - \omega$ Shear Stress Transport (SST) turbulence model is used to conduct the simulation. It is selected for its exceptional capabilities in analyzing external aerodynamics around the airfoils. This advanced model excels in boundary layer performance, providing excellent near-wall resolution while accurately predicting flow separation and capturing boundary layer transition effects critical for airfoil performance. Its hybrid approach represents a significant advantage, using the k-ω formulation in near-wall regions to directly resolve the viscous sublayer with dimensional variables and accurate wall stress predictions, while switching to the k-ε model in free-stream regions where its greater numerical stability and reduced computational intensity are beneficial. This combination captures the strengths of both models while mitigating their individual weaknesses. The SST model offers particular advantages for airfoil analysis through its superior prediction of adverse pressure gradients, crucial for accurately determining separation points and stall behavior. Additionally, it provides an optimal balance between computational efficiency and accuracy, allowing for comprehensive parametric studies within reasonable time frames while maintaining high-fidelity results for our analysis of the critical loads on the Lotus 49B wing structure.

3.4 Boundary conditions

The boundary condition configuration is set up to mimic a realistic simulation environment to accurately capture the aerodynamic phenomena experienced by a high-mounted F1 airfoil. The airfoil surface is defined with a no-slip condition, ensuring zero velocity at the wall and proper boundary layer development. Inflow velocity boundary conditions are applied to the left and top edges of the C-shaped domain, with a freestream velocity of 90 m/s (approximately 324 km/h), representative of high-speed sections at 1969 F1 circuits like Montjuic Park. The right boundary utilizes an outflow condition with zero gauge pressure, allowing for natural development of the wake region without artificial backpressure effects. Notably, we implement a no-slip condition on the bottom boundary with matching freestream velocity to simulate the moving ground beneath an F1 car, critical for capturing realistic ground effect interactions that significantly influence downforce generation and pressure distributions on the inverted airfoil [6].

3.5 Parameter sweep

The parameter sweep methodology systematically investigates the airfoil's performance across a wide range of operating conditions, spanning angles of attack from -20° to 20° in 1° increments. This comprehensive range allows us to capture the complete aerodynamic behavior from negative lift through zero angle, positive lift generation, and beyond the critical stall point, which for our reference NACA 0012 airfoil occurs at approximately 16° [7]. We anticipate similar stall characteristics in our simulation, enabling validation against established airfoil data. Each simulation is configured with stringent convergence criteria, allowing a maximum of 300 iterations with a convergence limit of 1e-6 to ensure solution accuracy. This parametric approach provides a thorough characterization of lift, drag, and moment coefficients across the entire operating envelope, crucial for identifying the critical loading conditions that potentially led to the catastrophic structural failures observed in the 1969 Spanish Grand Prix incidents.

3.6 Lift, drag, and moment calculation

The approach to calculating aerodynamic forces employs the fundamental principles of fluid dynamics, computing the lift and drag forces through direct integration of both pressure and viscous stress components over the airfoil surface. For each point on the airfoil surface, there is a traction force, f, which is a result of the pressure and viscous shear stress as follows:

$$f = \int (p+\tau) * \vec{n}\ dS = \begin{bmatrix} -p+\tau_{xx} & \tau_{xy} \\ \tau_{xy} & -p+\tau_{yy} \end{bmatrix} \begin{bmatrix} n_x \\ n_y \end{bmatrix} = \begin{bmatrix} (-p+\tau_{xx})n_x + \tau_{xy}n_y \\ \tau_{xy}n_x + \left(-p+\tau_{yy}\right)n_y \end{bmatrix} \qquad (1)$$

Where p is the pressure, τ is the viscous shear stress, n is the unit normal to the surface, and dS is the differential.

Then, drag and lift forces are computed once the airfoil boundary surface is computed as an integral of the traction force in the x and y direction respectively as follows [8]:

$$F_D = \int f * \widehat{e_x}\, dS \tag{2}$$

$$F_L = \int f * \widehat{e_y}\, dS \tag{3}$$

Where F_D is the drag force, F_L is the lift force, and e is the unit normal in the x and y directions.

Selecting each individual segment on the airfoil's surface and conducting line integration on the above equations yields the total lift and drag force [9]. For validation and comparison purposes, these forces are converted to the non-dimensional lift and drag coefficients by dividing by the dynamic pressure and reference area as follows:

$$C_D = \frac{F_D}{\frac{1}{2}\rho U^2 A} = \frac{F_D}{\frac{1}{2}\rho U^2 c} \tag{4}$$

$$C_L = \frac{F_L}{\frac{1}{2}\rho U^2 A} = \frac{F_L}{\frac{1}{2}\rho U^2 c} \tag{5}$$

Where C_D is the drag coefficient, C_L is the lift coefficient, ρ is the density, U is the air flow velocity, A is the reference area, and c is the chord length.

3.7 Center of pressure and moment about center of pressure

The center of pressure and associated moment calculations are critical for analyzing the structural loading on the wing support. In this case, we will approximate the center of pressure and center of mass to be located at 25% of the airfoil geometry's chord length given that there is little shift of the center of pressure between small angles.

And the moment is calculated as follows:

$$M_{COP} = \int (F_D * y - F_L * x)\ dS \tag{6}$$

Where M_{COP} is the moment about the center of pressure, y is the vertical distance between the center of pressure and drag force location on the airfoil and x is the horizontal distance between the center of pressure and lift force location on the airfoil.

For the purposes of the structural analysis, the support point is placed directly below the center of pressure at zero angle of attack, following the simplified approach described in Section 2.5. This configuration provides a conservative baseline for analyzing structural loading, as it minimizes the moment arm for the primary lift force while still accounting for moments induced by off-center pressure distributions at varying angles of attack.

4 Results and Discussion

4.1 Mesh convergence

Mesh convergence is conducted from the original COMSOL generated mesh to conduct mesh convergence. A refinement bounding box (4m x 2m) centered around the airfoil is defined for local refinement while keeping the global mesh the same size. This approach efficiently allocates computational resources to regions where flow gradients are steepest and most critical for accurate force prediction instead of areas far away from the airfoil. The incremental mesh refinements are shown in Figure __.

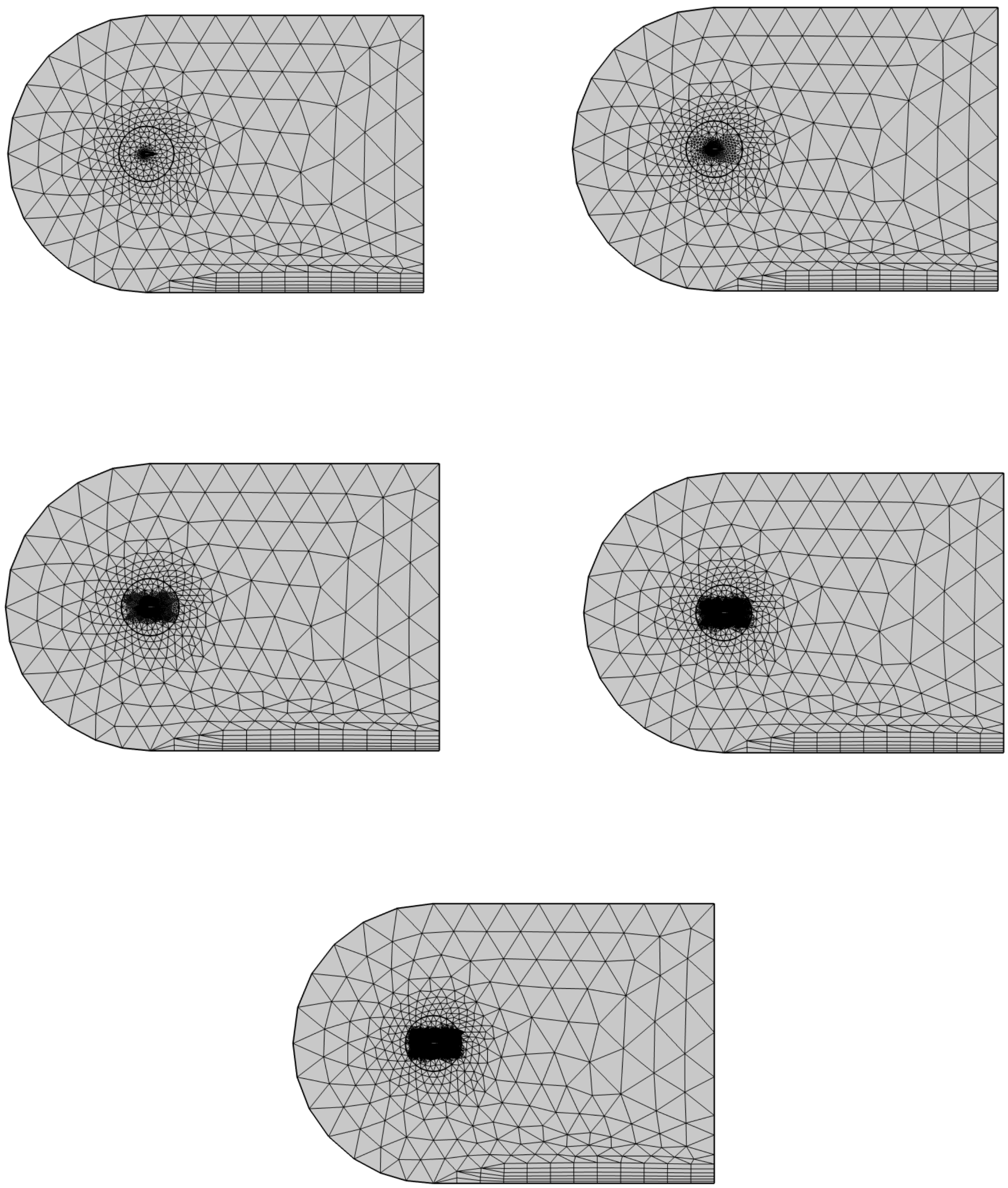

Figure __: Local mesh refinement with original mesh (top left), mesh 1 (top right), mesh 2 (middle left), mesh 3 (middle right), and mesh 4 (bottom)

In order to evaluate the results of the mesh convergence, a mesh sensitivity analysis is conducted. Converged simulation is characterized by the residual drop in 5 orders of magnitude in value for the velocity and pressure variables. To determine mesh convergence, the residual plots, lift coefficient, and drag coefficients are analyzed.

Table __ tabulates the results of the convergence study. Starting with the original mesh, it is progressively refined to meshes 1-4.

Table __: Lift and drag coefficient as a function of number of elements from mesh refinement at 0° angle of attack.

Mesh #	Number of elements	Time required to converge (s)	Lift coefficient	Drag coefficient	Relative error in CL (%)	Relative error in CD (%)
0 (no refinement)	965	3	-0.00220	0.039762	240.58	141.27
1	1705	11	0.00149	0.029367	4.79	78.20
2	4733	76	0.001501	0.021178	4.09	28.51
3	16793	306	0.001528	0.020148	2.36	22.26
4	64563	510	0.001565	0.01648	0	0

For the NACA 0012 airfoil at 0 degrees angle of attack, the mesh refinement shows clear convergence of both lift and drag coefficients. The lift coefficient converges to a value of 0.001565 with our finest mesh (mesh 4), which is very close to the theoretical value of 0 for a symmetric airfoil at zero angle of attack. This slight non-zero value (approximately 0.16% of the maximum lift coefficient) is within expected numerical accuracy limits and can be attributed to minor asymmetries in the computational mesh and rounding errors inherent to numerical solutions.

The drag coefficient converges to 0.01648 with mesh 4, which is slightly greater than published experimental values for the NACA 0012 at Reynolds number of 1,000,000 (around 0.007). This overestimation is consistent with known limitations of RANS turbulence models in predicting drag, particularly the skin friction component. However, the consistent trend of decreasing drag coefficient with mesh refinement indicates that the numerical solution is correctly capturing the underlying physics, even if absolute values have some systematic bias.

Despite the mesh refinement only being local to areas around the airfoil, the number of elements increases approximately 4 folds with each mesh refinement. Additionally, the time required to reach convergence increases with the mesh element as expected.

Figures __ to __ display the convergence plot for meshes 0 to 4 and are used to reveal important trends in solution stability.

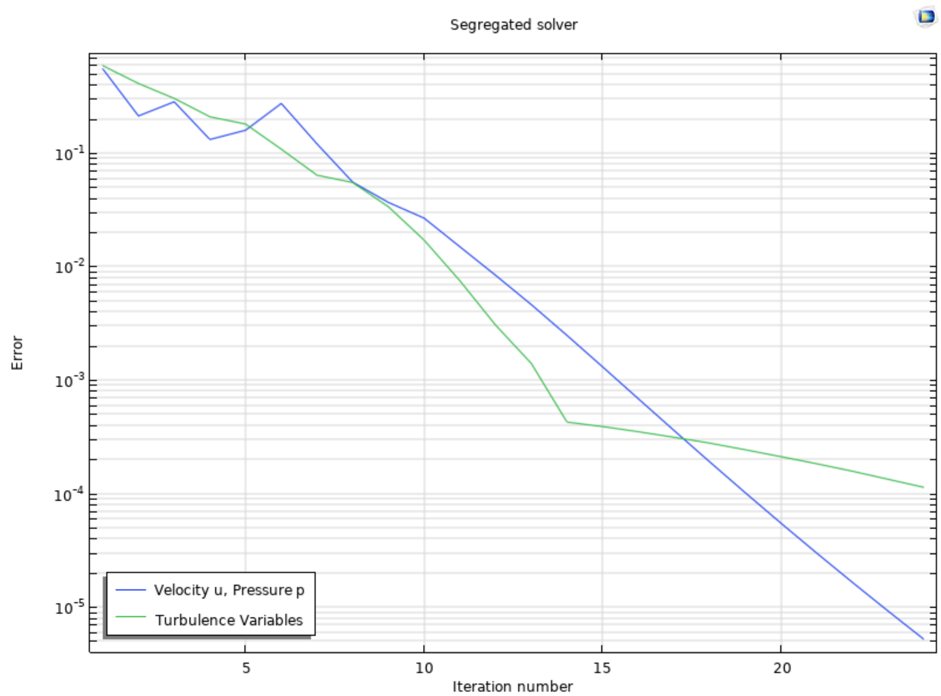

Figure __: Convergence plot for original mesh

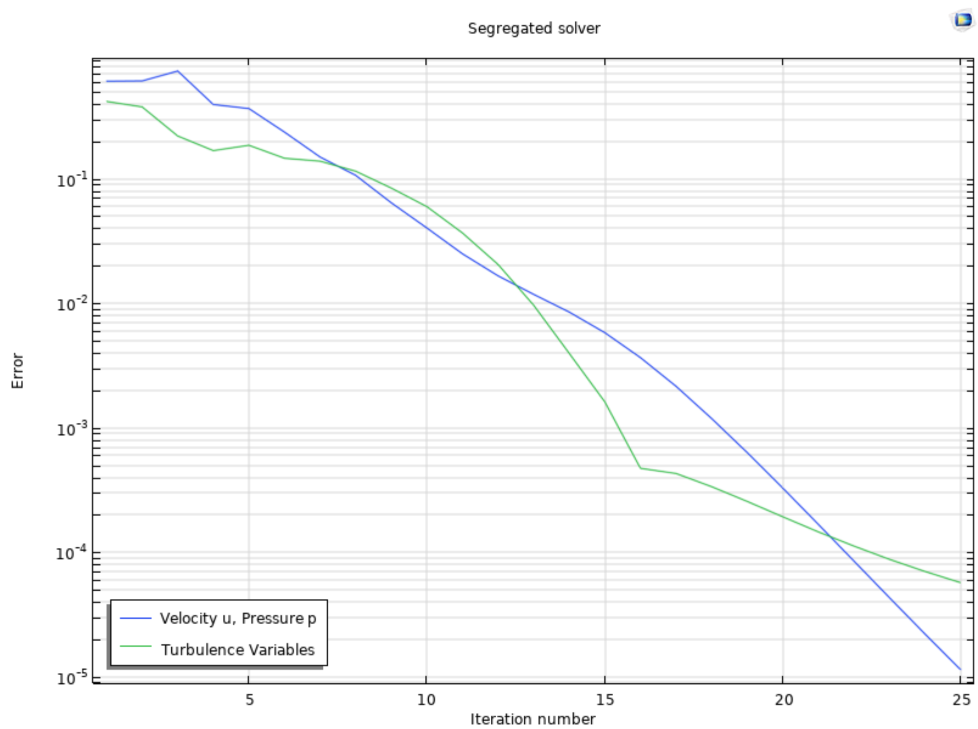

Figure __: Convergence plot for mesh #1

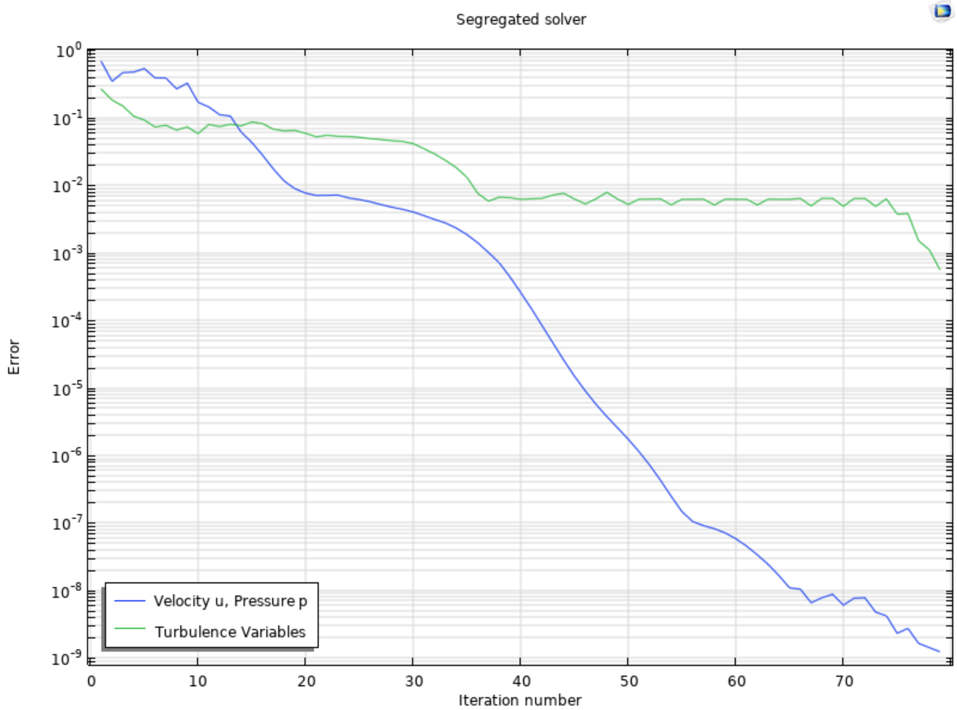

Figure __: Convergence plot for mesh #2

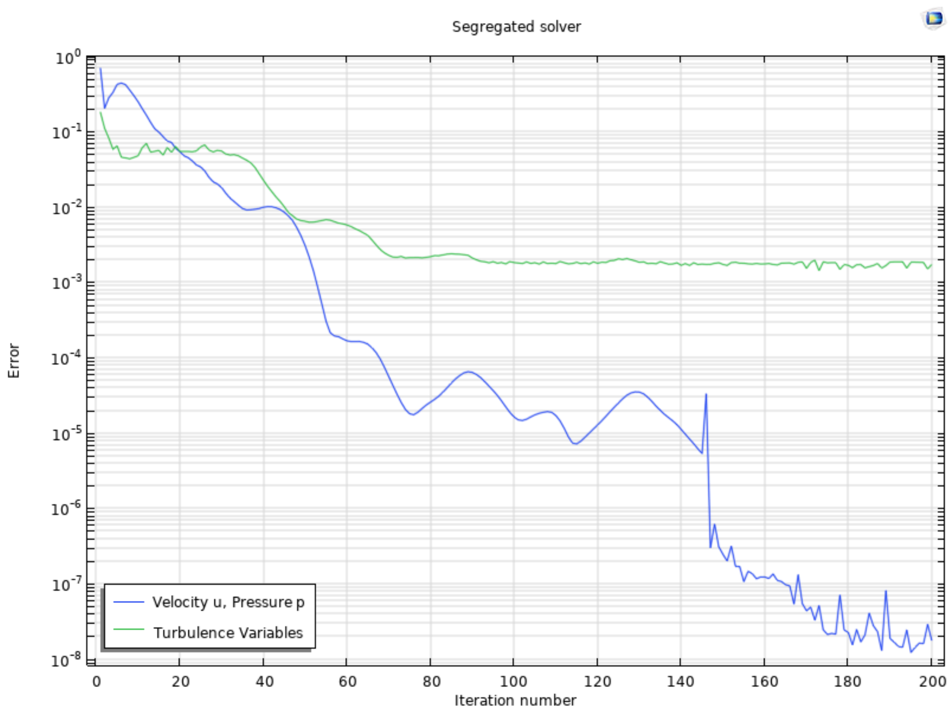

Figure __: Convergence plot for mesh #3

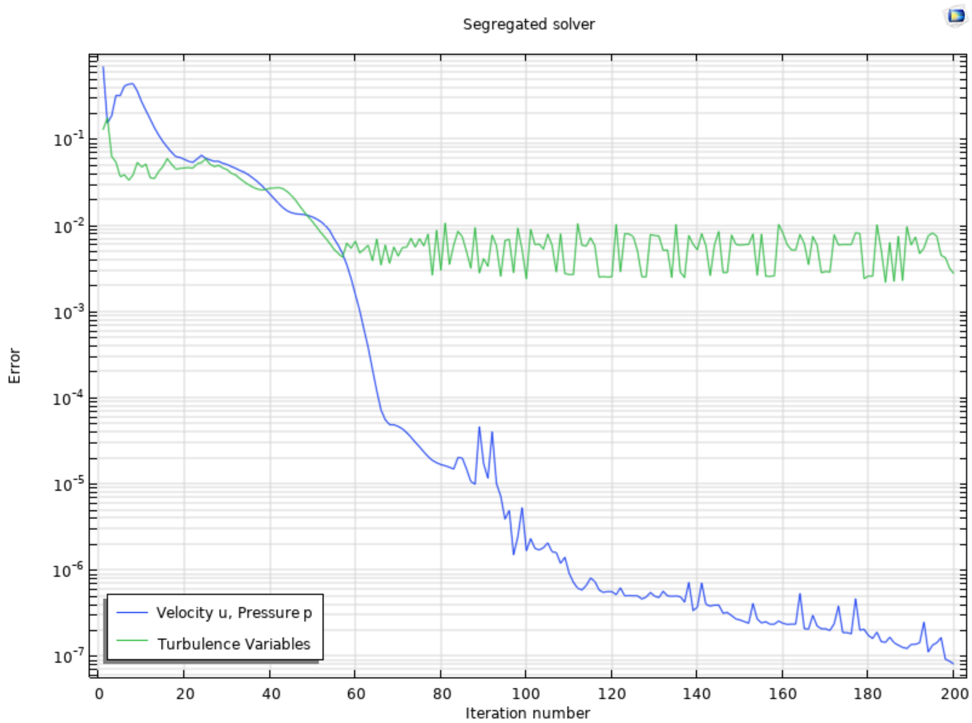

Figure __: Convergence plot for mesh #4

For the coarser meshes (original and mesh 1), residuals for velocity and pressure variables converge smoothly but with less accuracy, as evidenced by the relatively high errors in both lift and drag coefficients. As mesh density increases, particularly in meshes 2 through 4, more complex convergence behavior with minor oscillations is observed, yet ultimately reaching lower residual levels for the primary variables (velocity and pressure).

A notable observation is that turbulence variables (k and ω) consistently plateau at approximately 10^-2 across all mesh densities. This is an expected limitation of the k-ω SST model for external aerodynamics and does not significantly impact the primary results, as the aerodynamic forces are predominantly governed by pressure distributions that converge to much lower residual levels.

In order to find a balance between computation time and accuracy, the relative error in Cd and CL between when compared to mesh 4 is computed as mesh 4 is considered the most refined and accurate simulation result. Table __ displays the calculated relative error results.

Table __: Relative error in lift and drag coefficients between meshes

Mesh #	Relative error in CL (%)	Relative error in CD (%)
0	240.58	141.27

1	4.79	78.20
2	4.09	28.51
3	2.36	22.26
4	0	0

To quantitatively assess the impact of mesh refinement, the relative errors for lift and drag coefficients are calculated using mesh 4 as the reference as shown in Table __. The results show dramatic improvement from the original mesh to mesh 1, with the lift coefficient error decreasing from 240.58% to just 4.79%. Further refinements yield more modest improvements, with mesh 2 showing errors of 4.09% for lift and 28.51% for drag.

The notable disparity between lift and drag coefficient convergence rates with lift converging much faster than drag is consistent with CFD best practices. Drag prediction typically requires finer near-wall resolution to accurately capture boundary layer effects and separation phenomena, while lift is primarily governed by pressure distribution, which is less sensitive to mesh density.

Specifically, comparing the converged drag coefficient (CD ≈ 0.01648) to published NACA data (CD ≈ 0.007) shows that the simulation overestimates drag by a factor of approximately 2.35. This systematic bias is consistent across the simulations and is likely due to limitations in the turbulence modeling approach and near-wall mesh resolution. While this affects the absolute accuracy of the drag predictions, the relative changes in drag with angle of attack remain valid for our comparative analysis.

Based on this comprehensive mesh sensitivity analysis, mesh 2 is selected for all subsequent simulations. This mesh density provides an optimal balance between computational efficiency and solution accuracy, with lift coefficient errors below 5% and reasonable computation times. While mesh 3 and 4 offer incrementally better accuracy, the significant increase in computational cost (4× and 6.7× longer simulation times, respectively) does not justify the marginal improvement in accuracy for our parametric studies spanning multiple angles of attack.

4.2 NACA airfoil database comparison

Following the parameter sweep setup in Section 3.5, the lift and drag coefficients from the COMSOL simulation and NACA website are plotted against each other in Figures __ and __ respectively.

While F1 races can typically reach a top speed of 90 m/s, for comparison purposes, the inflow velocity in the COMSOL simulation is lowered to 15 m/s. The resulting Reynolds number is around 1,000,000, which is the same as the NACA database plots. Sample Reynolds number calculations are as follows:

$$Re = \frac{\rho U c}{\mu} \tag{8}$$

$$Re = \frac{1.225\frac{kg}{m^3} * 15\frac{m}{s} * 1m}{1.8 * 10^{-5}\frac{kg}{m * s}} = 1{,}020{,}833$$

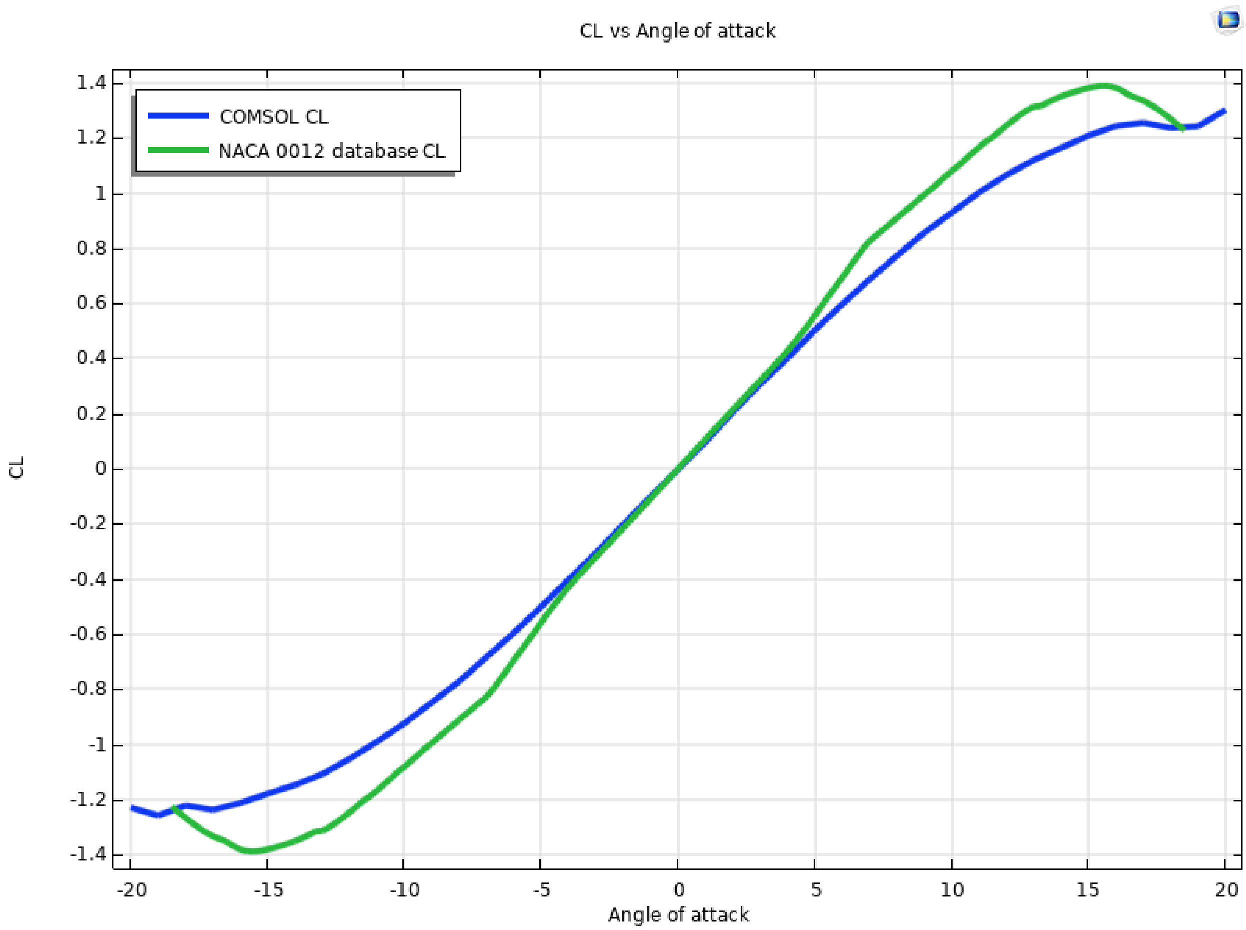

Figure 6 :Comparison of lift coefficient vs Angle of attack for NACA 0012 airfoil at Re=1,000,000

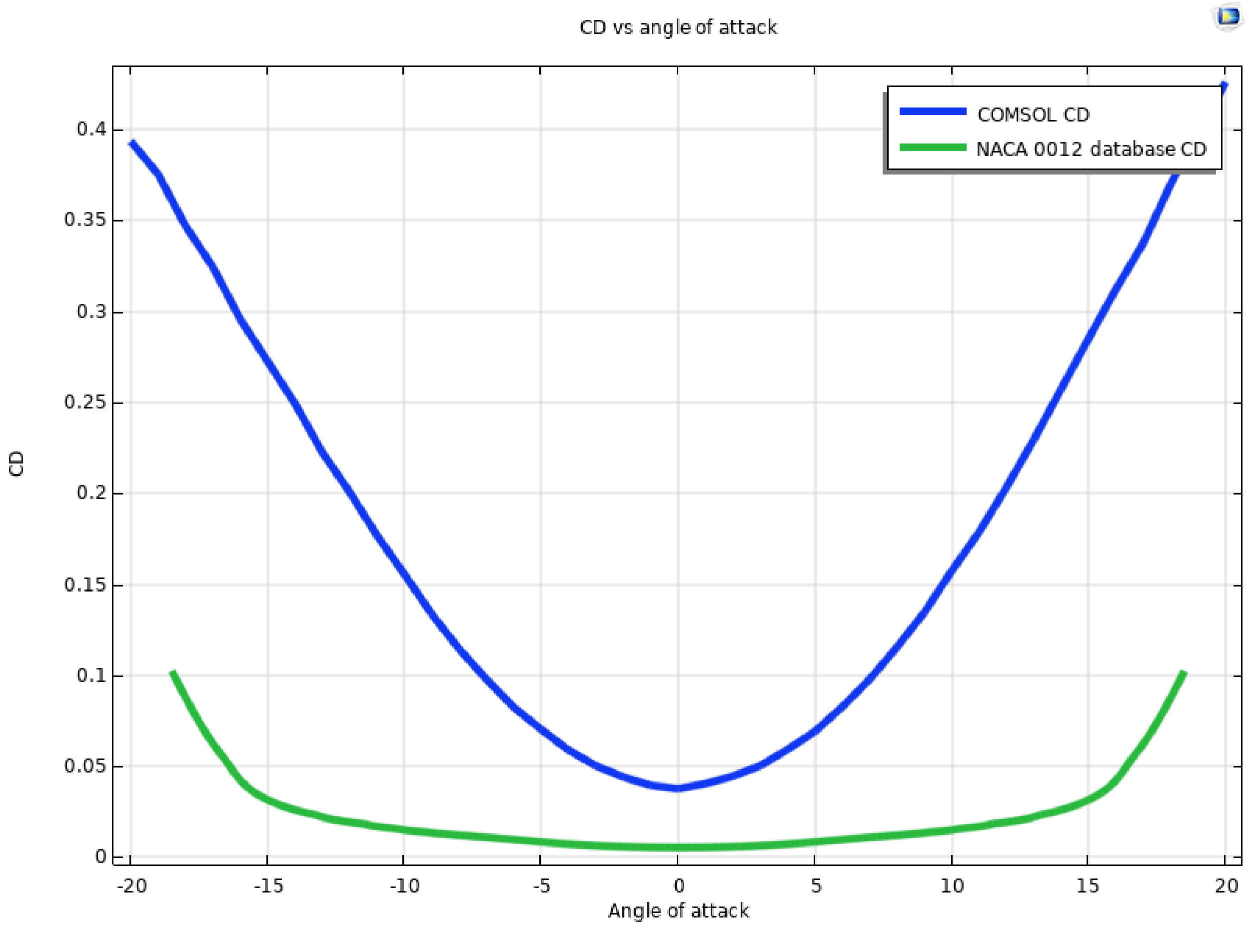

Figure 7: Comparison of drag coefficient vs Angle of attack for NACA 0012 airfoil at Re=1,000,000

The lift coefficient curve demonstrates strong correlation between the COMSOL simulation and reference NACA data. In the low angle of attack range (-5° to 5°), the simulation closely tracks the reference data, with both curves showing nearly identical slopes. This excellent agreement in the linear region validates the model's ability to capture the fundamental lift-generating mechanisms.

The simulation accurately predicts the stall angle at approximately 16°, consistent with the published data. However, the simulation shows a slightly lower maximum lift coefficient ($C_{L,max} \approx 1.25$) compared to the reference value ($C_{L,max} \approx 1.4$). This discrepancy is likely due to the limitations of steady-state RANS modeling in capturing the complex unsteady separation phenomena that occur at high angles of attack.

At 0° angle of attack, the simulation correctly predicts near-zero lift, which is expected for a symmetric airfoil like the NACA 0012. At negative angles of attack, the performance nearly mirrors positive angles of attack, which is also expected for symmetric airfoils.

The drag coefficient curve demonstrates more significant discrepancies between the simulation and reference data than the lift coefficient curve. The simulation consistently predicts higher drag coefficients across all angles of attack. At zero angle of attack, the simulated CD ≈ 0.04 compared to the reference CD ≈ 0.007. This disparity increases at higher angles of attack.

Despite the discrepancy in absolute values, the overall trend of the drag curve matches the reference data, showing the characteristic U-shaped profile with minimum drag at 0° and increasing values as the angle deviates in either direction.

At extreme angles (±20°), the simulation shows CD ≈ 0.45 compared to reference values of CD ≈ 0.1. This significant overestimation is likely due to limitations in accurately predicting separated flow regions, which dominate drag production at high angles of attack.

Despite slight limitations in absolute drag prediction, the excellent agreement in lift characteristics and the correct prediction of drag trends provide sufficient confidence for the analysis of structural loading on the wing supports. The lift forces, which are accurately captured by the model, would have been the primary contributor to the bending moments that likely caused the structural failures observed in the 1969 Lotus 49B.

4.3 Support torque setup and calculation

Unlike the freestream validation setup presented in Section 4.2, this section analyzes the aerodynamic behavior of the airfoil in a near-ground configuration that better reflects the conditions of a high-mounted Formula 1 wing. The aim is to evaluate the aerodynamic torque experienced by the structural support located below the airfoil, specifically under conditions representative of the 1969 Lotus 49B design.

The domain is a 2D C-shaped region approximately 20 meters wide, designed to minimize blockage and wake reflection. The airfoil, with a chord length of c=1m, is positioned 1.2 meters above the lower boundary, simulating the mounting height above the chassis. The boundary conditions are described in Section 3.4. This configuration intentionally differs from standard wind tunnel tests, which typically use freestream inlets on all sides and assume no ground interference. Consequently, aerodynamic coefficients derived here reflect ground-effect influences absent in typical NACA data.

The Reynolds number calculated from the given density, viscosity and velocity is 6.125x10^6. This number places the flow firmly within the fully turbulent regime, justifying the use of turbulence models (SST k−ω) without needing laminar-turbulent transition modeling. Turbulent kinetic energy and specific dissipation rate at the inlet were defined consistently with the free-stream parameters.

To ensure solution reliability, a systematic mesh refinement study was conducted. Five levels of refinement were tested, ranging from ~3,800 to ~670,000 elements.

Mesh #	Number of elements	Time required to converge (s)	Lift coefficient	Drag coefficient
0 (no refinement)	3887	8	3.0982E-4	0.0067325
1	11720	13	-9.9621E-5	0.0073753
2	43152	38	-4.6553E-4	0.0071383
3	168608	195	-9.2634E-4	0.0072831
4	669398	987	-9.1686E-4	0.0073207

Both Cl and Cd exhibited asymptotic convergence behavior. Changes beyond Mesh 2 were small compared to the massive increases in computational cost. Therefore, Mesh #1 (11,720 elements**)** was selected as a balanced choice for sweeping multiple angles of attack efficiently while capturing accurate aerodynamic behavior.

The goal is to calculate the aerodynamic torque transmitted to the structural base (i.e., the beam support located 3 meters below the airfoil's center of gravity). This includes both the moment caused by distributed aerodynamic forces and the additional torque due to force offsets from the mounting position.

We first define our reference frame. The airfoil's center of pressure(CP) is placed at the origin (0,0). The beam's support point is at (0, −1.2), vertically 1.2 meters below the CP. We then locate lift and drag forces using the methodology already discussed in previous sections. After acquiring the moment at the center of pressure. We then calculate the moment at the end of the support beam using the following equation:

$$M_{\text{beam}} = M_{\text{CG}} + 1.2 \cdot F_D$$

Utilizing the previously described techniques and calculations, we obtain the following plots that show key characteristics of the airfoil:

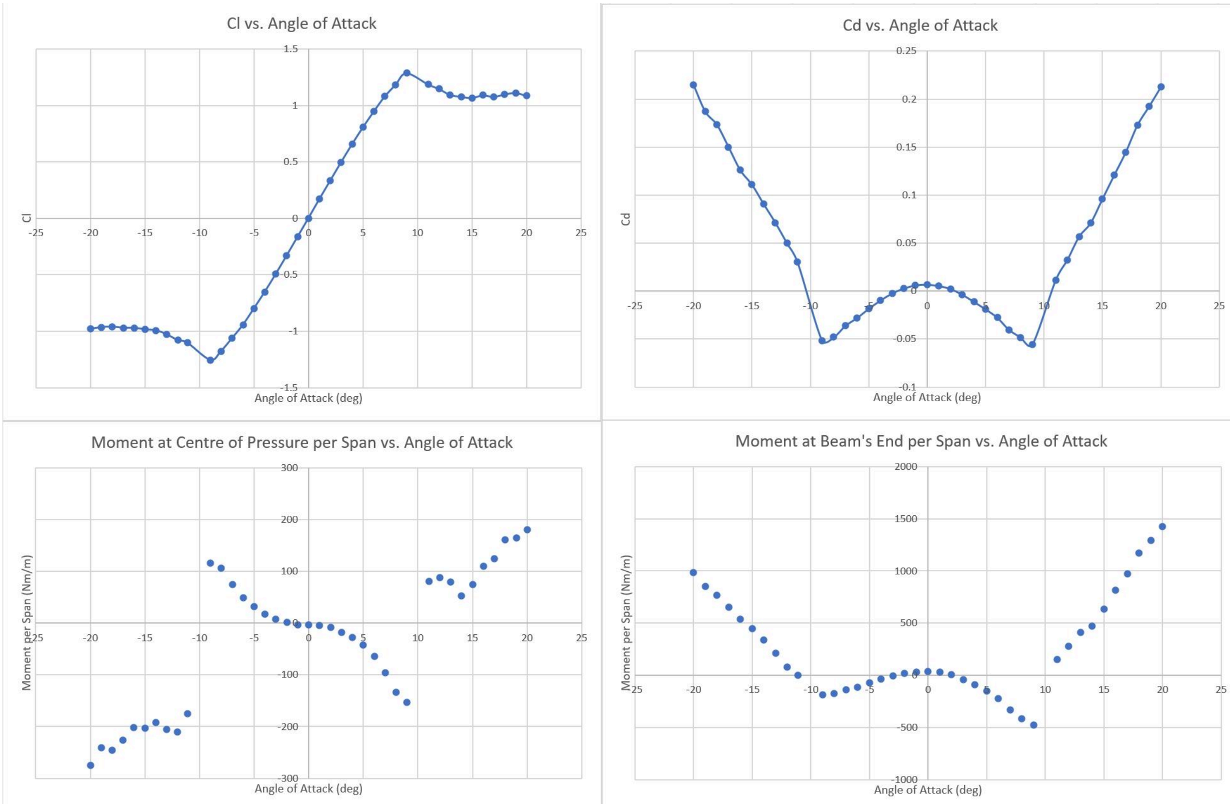

Figure : Cl vs. AoA, Cd vs. AoA, M of CoP vs. AoA, M at Beam's End vs. AoA

The computed lift and drag coefficients across angles of attack α from −20deg to +20deg show clear ground-effect influence.

- The Cl curve is non-symmetric around α=0, indicating distortion from ground interference.
- Maximum lift occurs near α=9, after which stall-like behavior and a plateau in Cl are observed.
- The drag curve Cd is U-shaped but elevated compared to classical NACA results (e.g., minimum Cd ≈ 0.03–0.04 instead of 0.01–0.02). This increase is attributed to ground-effect pressure build-up, boundary layer growth, and early flow separation due to the ground wall.

Two moments were also calculated:

- Moment at Center of Pressure (CP) — based on a common industrial practice on symmetric airfoils that places CP at ¼ of the chord length from the tip.

- Moment at Beam Support (1.2 meters below CP) — includes additional torque from horizontal drag force offset.

Both moment curves showed dramatic nonlinearity around $\alpha=9-10$. A sharp change in direction and magnitude occurred between $\alpha=9$ and 10.

One of the most noticeable differences between this study and classical NACA wind tunnel results lies in the shape of the drag coefficient curve Cd as a function of angle of attack α. In canonical NACA data, particularly for symmetric airfoils such as the NACA 0012, the Cd–α curve is smooth, parabolic, and symmetric about $\alpha=0$. Minimum drag occurs near zero angle, and drag increases steadily and symmetrically with increasing magnitude of α due to rising pressure and form drag from flow separation at higher angles.

However, in the present simulation, the Cd curve shows a broad, flat region — or “bulk” — spanning approximately $\alpha=-10$ to $+10$, with elevated drag values compared to NACA results in that range. This difference is not a numerical error or mesh artifact (as shown by mesh independence), but rather the result of fundamental physical and geometric differences between the experimental and simulated setups.

One of the most noticeable differences between this study and classical NACA wind tunnel results lies in the shape of the drag coefficient curve Cd as a function of angle of attack α. In canonical NACA data, particularly for symmetric airfoils such as the NACA 0012, the Cd–α curve is smooth, parabolic, and symmetric about $\alpha=0$. Minimum drag occurs near zero angle, and drag increases steadily and symmetrically with increasing magnitude of α due to rising pressure and form drag from flow separation at higher angles.

However, in the present simulation, the Cd curve shows a broad, flat region — or “bulk” — spanning approximately $\alpha=-10$ to $+10$, with elevated drag values compared to NACA results in that range. This difference is not a numerical error or mesh artifact (as shown by mesh independence), but rather the result of fundamental physical and geometric differences between the experimental and simulated setups.

Another contributing factor is the turbulent boundary layer and wake dynamics. While NACA wind tunnel data often include transition control or operate at conditions close to laminar, this simulation assumes fully turbulent flow at a Reynolds number of $Re\approx6.1\times10^{6}$, This means:

- Boundary layer separation occurs more gradually, but earlier than in a controlled tunnel.
- Wake thickness remains higher across a wider range of α.
- Viscous shear and mixing layers near the wall increase base drag even at modest angles.

These effects collectively dampen the parabolic shape and raise the floor of the Cd curve in the mid-angle range.

Visual inspection of the velocity and vorticity fields shows persistent wake structures and vortex shedding around the trailing edge at $-10<\alpha<10$. These vortices, enhanced by the wall-induced asymmetry, lead to higher pressure recovery losses and broadened wake width — both of which raise drag significantly compared to smooth flow in symmetric NACA setups.

It is also observed that as α increases toward +10, a sharp increase in both drag and moment occurs, while classical NACA data shows smooth transition toward stall. This supports the hypothesis that ground proximity increases stall sensitivity, causing flow instability and drag rise even before classical stall conditions are reached.

Based on the aerodynamic analysis, It is likely that the design team chose an operating angle near $\alpha=9$, where maximum downforce (lift) was achieved. However, even a slight operational deviation (e.g., due to track bumps or steering inputs) moving from $\alpha=9$ to $\alpha=10$ results in a large moment jump. This rapid moment fluctuation could apply transient, amplified torques to the wing supports, accelerating fatigue crack growth or causing instantaneous mechanical failure. The use of slender aluminium struts and limited understanding of dynamic aeroelastic loads in 1969 would exacerbate this risk.

- COMSOL changes
    - Change to 90m/s, take the angle of attack that yielded the greatest lift (since that is most likely what the racers used for their races, or find a common angle of attack from online) from plots in 4.1

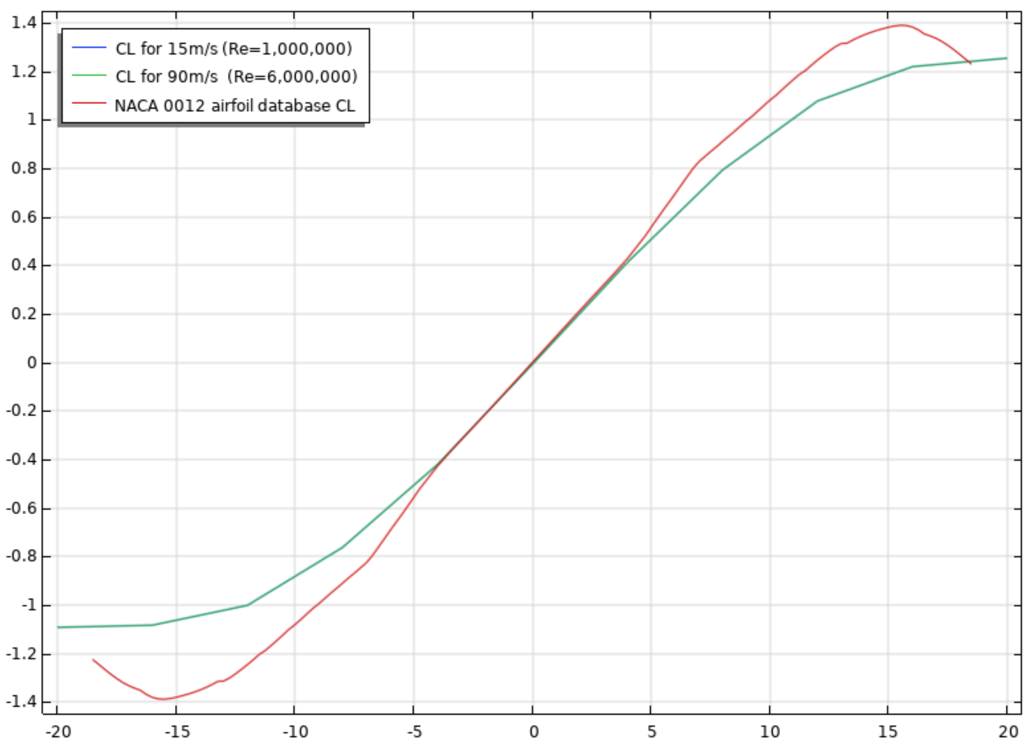
CL for 15m/s (Re=1,000,000)
CL for 90m/s (Re=6,000,000)
NACA 0012 airfoil database CL
1.4
1.2
1
0.8
0.6
0.4
0.2
0
-0.2
-0.4
-0.6
-0.8
-1
-1.2
-1.4
-20
-15
-10
-5
0
5
10
15
20

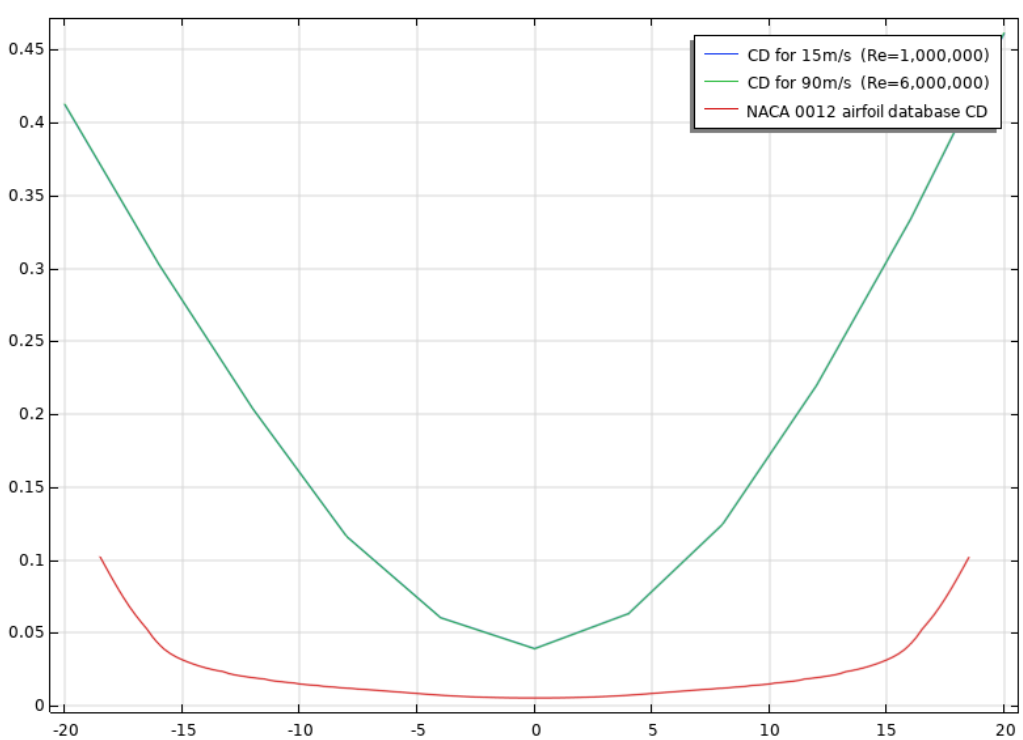
CD for 15m/s (Re=1,000,000)
CD for 90m/s (Re=6,000,000)
NACA 0012 airfoil database CD
0.45
0.4
0.35
0.3
0.25
0.2
0.15
0.1
0.05
0
-20
-15
-10
-5
0
5
10
15
20

Using mesh #1

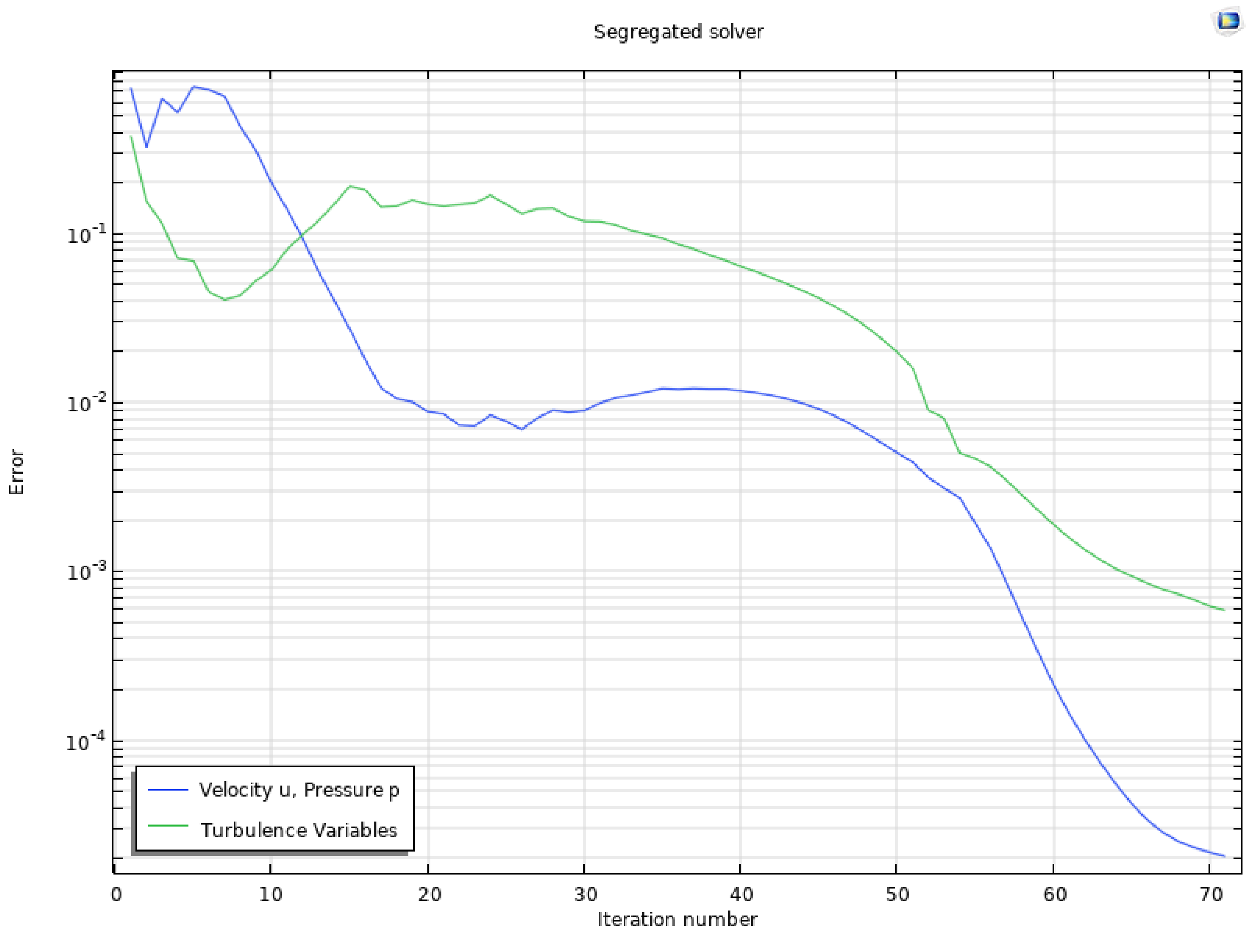

Figure : Convergence plot for mesh #0

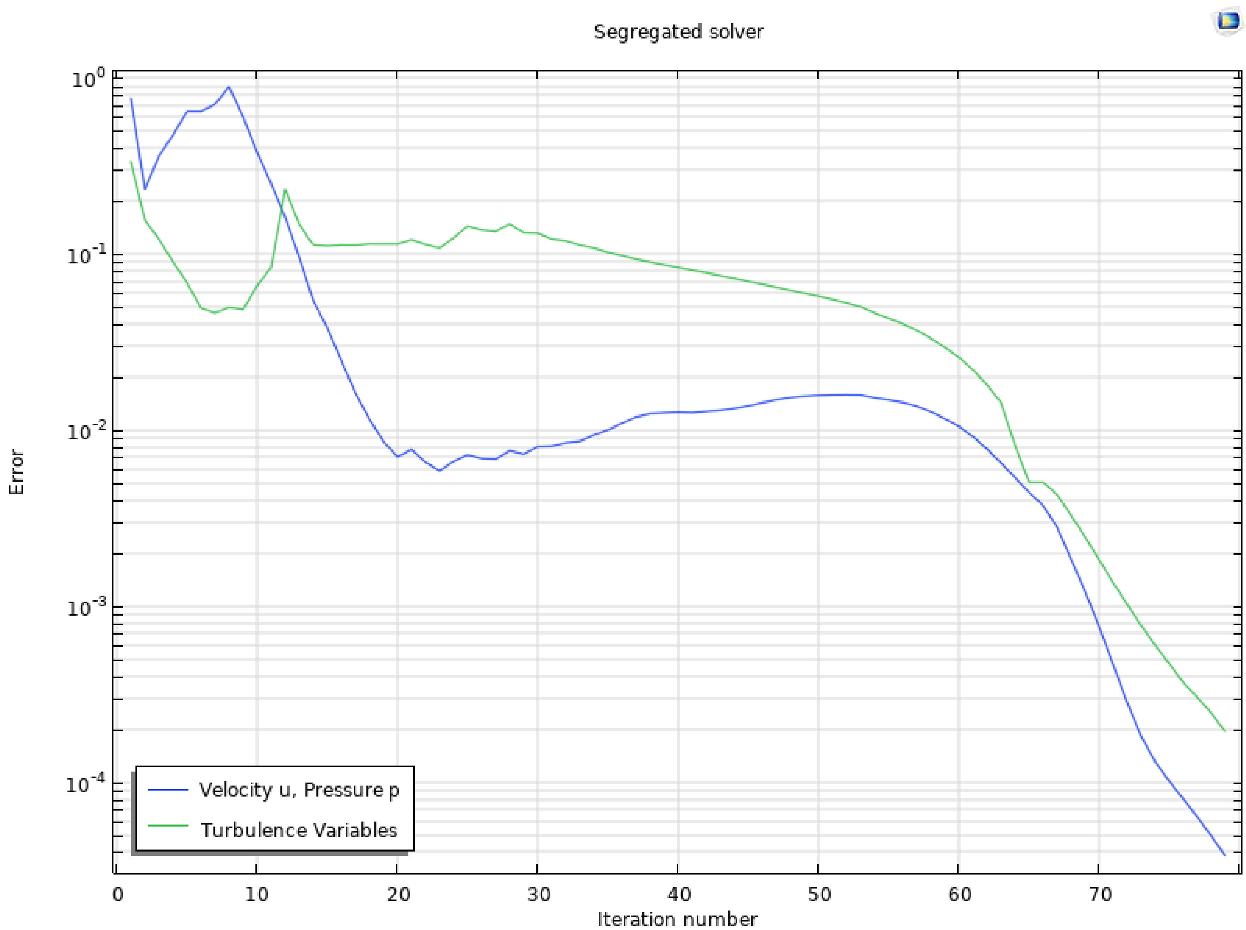

Figure : Convergence plot for mesh #1

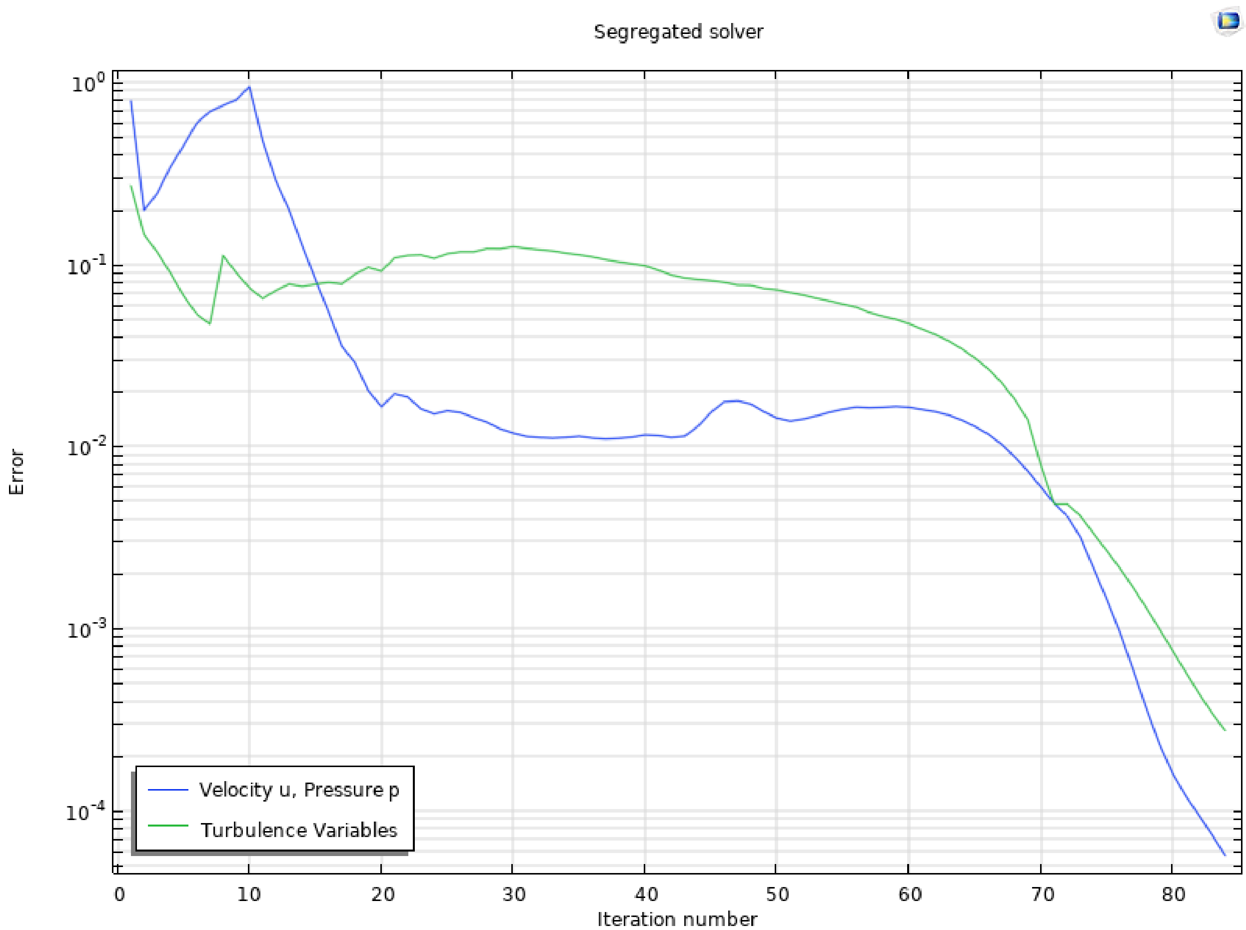

Figure : Convergence plot for mesh #2

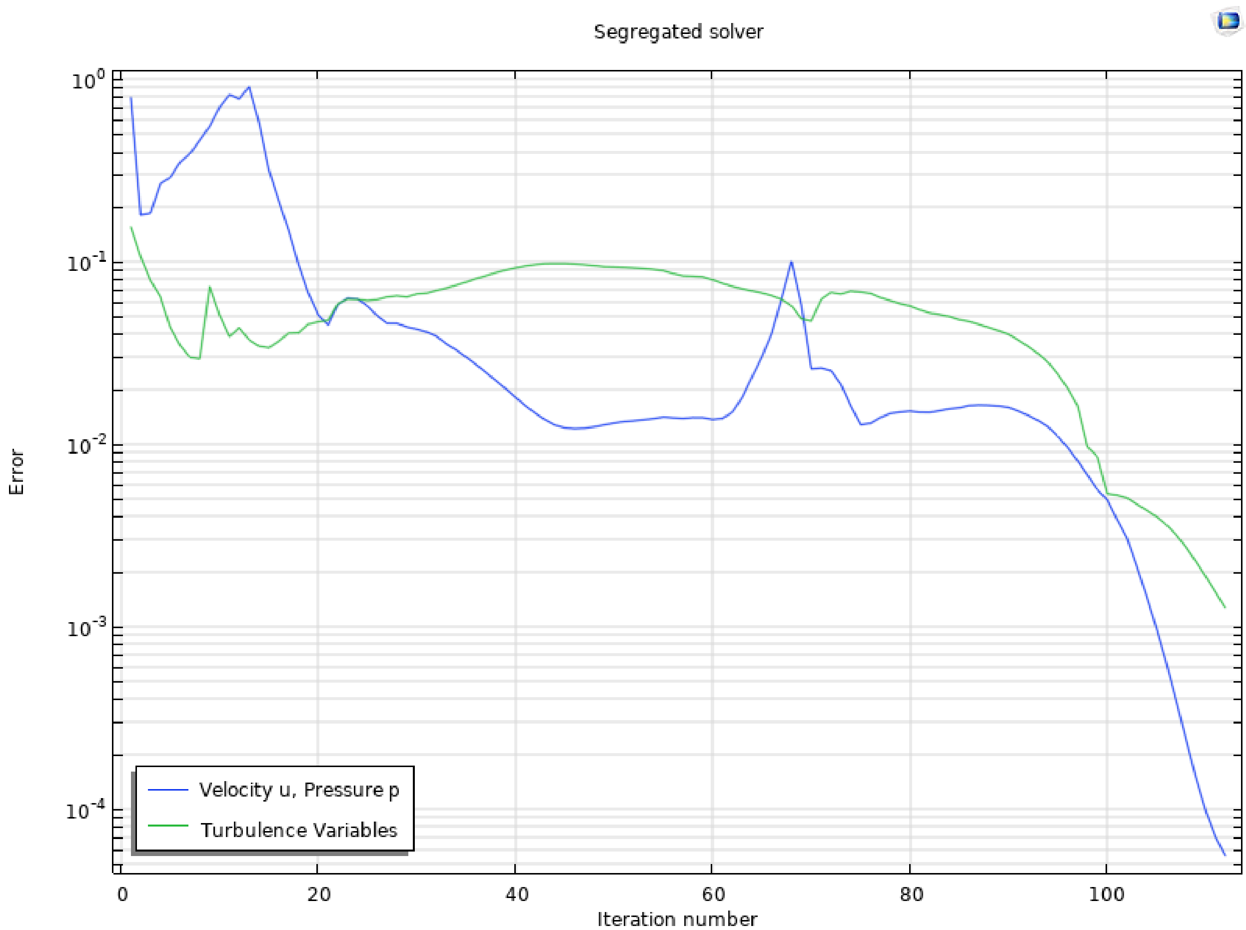

Figure : Convergence plot for mesh #4

5 Conclusion

- Is it possible for the forces to break the support?
- Reflect back on our assumptions and if they were reasonable. Did they make or break our conclusion

6 Future work

- Limitations of our assumptions and setup

7 References

[1] https://vintageaviationnews.com/warbird-articles/evolution-of-an-airfoil.html

[2] https://petroleummuseum.org/chaparral-2e/

[3] https://onmotorsport.substack.com/p/the-rise-and-fall-of-f1s-high-wings

[4]https://www.researchgate.net/figure/NACA-4412-122-Rear-Wing-Airfoil-NACA-2408-Due-to-location-of-engine-at-the-rear-end-of_fig1_277346887

[5] https://en.wikipedia.org/wiki/Lotus_49

[6]https://essengoldparts.com/blog/2024-aluminum/#:~:text=By%20the%201960s%2C%202024%20had,required%20great%20strength%20and%20durability.

[7]https://www.researchgate.net/figure/Details-of-the-airfoil-computational-domain_fig20_337282607

[8]http://airfoiltools.com/search/index?m%5Bgrp%5D=naca4d&m%5Bsort%5D=1

[9] https://www1.grc.nasa.gov/beginners-guide-to-aeronautics/lift-to-drag-ratio/

[10] https://www.comsol.com/blogs/how-do-i-compute-lift-and-drag

[11] https://forums.autosport.com/topic/127678-top-speeds-from-the-1960s-70s-80s/

[12] https://www.rotaryforum.com/threads/cg-for-0012-airfoil.1136129/

[13] https://www.comsol.com/model/flow-around-an-inclined-naca-0012-airfoil-14629

8 Appendix